J. Fluid Mech. (2005), *vol.* 541, *pp.* 91–104.
doi:10.1017/S0022112005005847 Printed in the United Kingdom

Analysis of transitions between fluttering, tumbling and steady descent of falling cards

By A. ANDERSEN[1], U. PESAVENTO[2] AND Z. JANE WANG[1]

[1]Cornell University, Department of Theoretical and Applied Mechanics, Ithaca, NY 14853, USA

[2]Cornell University, Department of Physics, Ithaca, NY 14853, USA

(Received 12 August 2004 and in revised form 25 April 2005)

We study the dynamics of a rigid card falling in air using direct numerical simulations of the two-dimensional Navier–Stokes equation and a fluid force model based on ordinary differential equations derived from recent experiments and simulations. The system depends on three non-dimensional parameters, i.e. the thickness-to-width ratio, the dimensionless moment of inertia, and the Reynolds number. By increasing the thickness-to-width ratio in the direct numerical simulations and thereby the non-dimensional moment of inertia we observe a transition from periodic fluttering to periodic tumbling with a wide transition region in which the cards flutter periodically but tumble once between consecutive turning points. In the transition region the period of oscillation diverges and the cards fall vertically for distances of up to 50 times the card width. We analyse the transition between fluttering and tumbling in the ODE model and find a heteroclinic bifurcation which leads to a logarithmic divergence of the period of oscillation at the bifurcation point. We further discuss the bifurcation scenario of the ODE model in relation to our direct numerical simulations and the phase diagrams measured by Willmarth, Hawk & Harvey (1964) and Belmonte, Eisenberg & Moses (1998).

1. Introduction

Leaves, tree seeds, and paper cards falling in air are spectacular examples of time-dependent fluid dynamics at intermediate Reynolds numbers at which both inertial and viscous effects are important. The trajectory of a falling card typically appears to be very complex with the card either oscillating from side to side (fluttering) or rotating and drifting sideways (tumbling). Despite fluttering and tumbling being common everyday phenomena that have interested scientists for centuries, see the qualitative discussion of tumbling by Maxwell (1854), little is known theoretically about the nature of the transitions between fluttering, tumbling, and steady descent.

Willmarth, Hawk & Harvey (1964) measured a phase diagram for falling disks with fluttering, tumbling, and steady descent. Both the three-dimensional motion of a falling circular disk and the two-dimensional motion of a falling card depend on six dimensional quantities, i.e. the diameter or the width of the object, $2a$, the thickness of the object, $2b$, the density of the object, ρ_s, the density of the fluid, ρ_f, the kinematic viscosity of the fluid, ν, and the acceleration due to gravity, g. From the six dimensional quantities it is possible to form three non-dimensional numbers. The phase diagram was constructed using the ratio between the thickness and the diameter of the disk, β, the dimensionless moment of inertia, I^*, and the Reynolds number, Re. The experiment focused on the small-β limit in which the

dynamics is independent of β and the phase diagram depends on Re and I^* alone. The disks fall steadily and broadside on for Re below 100, and for larger values of Re they flutter when I^* is small and tumble when I^* is large. Field *et al.* (1997) made further experiments on falling disks and found a chaotic transition region between fluttering and tumbling, Smith (1971) measured a qualitatively similar phase diagram for falling plates, and Belmonte, Eisenberg & Moses (1998) studied the transition from fluttering to tumbling with increasing I^* in a quasi-two-dimensional experiment with a narrow container in which the plate motion was constrained mechanically to be two-dimensional. Andersen, Pesavento & Wang (2005) measured the trajectories of fluttering and tumbling plates using a quasi-two-dimensional setup and obtained the instantaneous fluid forces from the measured accelerations. In the experiment the plates were released in a water tank and allowed to fall freely without any constraints on their motion. The plate length was much longer than its width and thickness, and the plates were released so that they rotated about their long axis. Three-dimensional effects at the tips were therefore negligible in the experiment, and the motion was effectively two-dimensional.

In this paper we describe the phase diagram and the transitions using direct numerical simulations of the two-dimensional Navier–Stokes equation and a fluid force model based on ordinary differential equations derived from recent direct numerical simulations (Pesavento & Wang 2004) and experiments (Andersen *et al.* 2005). By increasing the thickness-to-width ratio and thereby the dimensionless moment of inertia we find a transition between periodic fluttering and periodic tumbling. We observe a wide transition region with periodic motion in the direct numerical simulations and compare the findings with the apparently chaotic trajectories observed in the quasi-two-dimensional experiment on falling plates by Andersen *et al.* (2005) and the chaotic transition region found in the three-dimensional experiments on falling disks by Willmarth *et al.* (1964) and Field *et al.* (1997).

The fluid force model, which contains both translational and rotational lift, was introduced by Pesavento & Wang (2004) and compared favourably with experimental results by Andersen *et al.* (2005). We discuss the assumptions and the limitations of the theoretical model and the difference between the current model and existing models proposed by Tanabe & Kaneko (1994), Mahadevan (1996), and Belmonte *et al.* (1998). We show that the model depends naturally on the three non-dimensional parameters suggested by Willmarth *et al.* (1964). The model has two different steady solutions in which the card falls edge on and broadside on, respectively. The edge-on fixed point is always unstable, whereas we find a transition between steady broadside-on descent and oscillatory motion via a supercritical Hopf bifurcation in which the broadside-on fixed point changes stability. We further analyse the transition between fluttering and tumbling in the fluid force model and show that the transition is a heteroclinic bifurcation which leads to a logarithmic divergence of the period of oscillation at the bifurcation point. We conclude the paper with a comparison of the bifurcation scenarios of the fluid force model and the direct numerical simulations.

2. Direct numerical simulations of fluttering and tumbling

2.1. *Numerical method*

We solve the two-dimensional Navier–Stokes equation for the flow around a rigid plate with elliptical cross-section falling freely in a fluid. We use a computational method which is similar to the technique applied by Wang (2000) for the two-dimensional flow around a flapping wing with prescribed kinematics. The method makes use of the

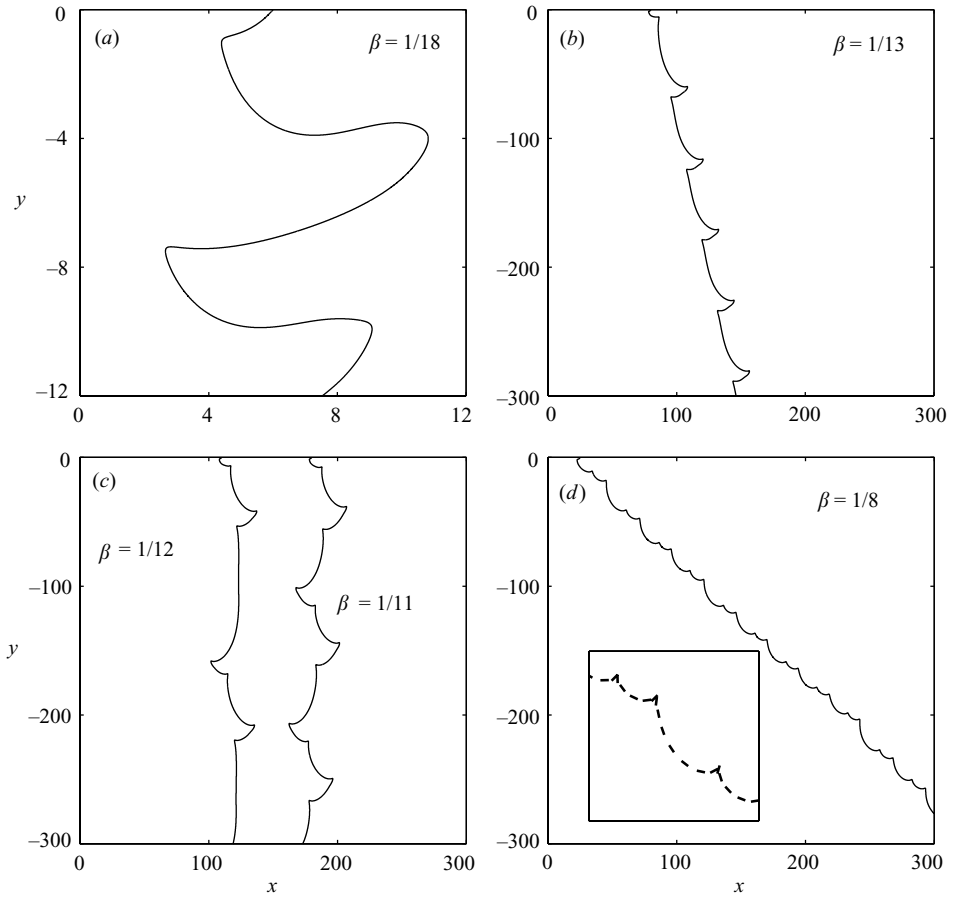

FIGURE 1. Trajectories obtained from direct numerical simulations of the two-dimensional Navier–Stokes equation for freely falling plates in the transition range between fluttering and tumbling: (*a*) periodic fluttering with the non-dimensional period of oscillation $T = 8.1$, (*b*) fluttering close to the transition between fluttering and tumbling with $T = 17.3$, (*c*) mixture of fluttering and tumbling with $T = 34.1$ for $\beta = 1/11$ and $T = 43.4$ for $\beta = 1/12$, and (*d*) periodic tumbling with $T = 12.1$. The semi-major axes of the plates have unit length in the four plots, and the periods of oscillation are made non-dimensional as described in § 4.

vorticity–stream function formulation and a body-fitted computational grid generated by a conformal mapping. The method and its adaptation to model freely falling plates is described in detail in Pesavento & Wang (2004) and Andersen *et al.* (2005).

2.2. *Solutions in the transition range between fluttering and tumbling*

Figure 1 shows a family of trajectories with different thickness-to-width ratio, which range from periodic fluttering with $\beta = 1/18$ in figure 1(*a*) to periodic tumbling with $\beta = 1/8$ in figure 1(*d*). The density ratio was $\rho_s/\rho_f = 2.05$ in the simulations and the Reynolds number based on the semi-major axis and the average descent speed was between 400 and 600. The trajectories in figures 1(*a*) and 1(*d*) are similar to the periodic trajectories measured by Andersen *et al.* (2005) and alternate between gliding at low angle of attack and fast rotational motion at the turning points. In the parameter range between periodic fluttering and periodic tumbling we observe a transition region with either asymmetric fluttering, as shown in figure 1(*b*), or

solutions in which the plate flutters in an apparently periodic fashion but tumbles once between consecutive turning points as shown in figure 1(*c*).

A characteristic feature of the dynamics in the transition region is that the plates fall vertically and edge on for long distances as shown for $\beta = 1/12$ in figure 1(*c*). The time spent in the vertical edge-on descent is much longer than the time spent gliding in periodic fluttering and periodic tumbling outside the transition region as shown in figures 1(*a*) and 1(*d*). The length of the vertical descent and therefore the period of oscillation diverges in the transition region. The periods of oscillation are reported in non-dimensional form in the caption of figure 1 for comparison with the results of the non-dimensional quasi-steady model in § 6.2. We find that the period of oscillation increases by a factor of 5 in the transition region relative to the period of oscillation for fluttering and tumbling outside the transition region, but due to the large computational cost in the transition region we have not been able to determine the precise functional form of the divergence based on our direct numerical simulations.

2.3. *Direct numerical solutions versus previous experiments*

The presence of a transition region between periodic fluttering and periodic tumbling is in agreement with the quasi-two-dimensional experiment on falling plates by Andersen *et al.* (2005), but in disagreement with the quasi-two-dimensional experiment by Belmonte *et al.* (1998) in which a sharp transition is found. We speculate that the sharp transition observed by Belmonte *et al.* (1998) arises because the quasi-two-dimensional flow is established using a narrow flow tank in which the falling plates touch the container walls in order to constrain their motion to be two-dimensional. Another qualitative difference between the two experiments is related to centre of mass elevation. The trajectories reported by Belmonte *et al.* (1998) do not display centre of mass elevation, whereas we find numerically (Pesavento & Wang 2004) and experimentally (Andersen *et al.* 2005) that the centre of mass is elevated at the turning points in fluttering and tumbling. We speculate that the absence of center of mass elevation in the experiment by Belmonte *et al.* (1998) is due to friction between the plates and the container walls. In the experiment by Andersen *et al.* (2005) such additional damping is not present, since the plates fall without touching the container walls.

The direct numerical simulations show that the transition between periodic fluttering and periodic tumbling does not always take place through a sequence of apparently chaotic states like the trajectories observed in the quasi-two-dimensional experiment by Andersen *et al.* (2005) and in the three-dimensional experiments on circular disks by Willmarth *et al.* (1964) and Field *et al.* (1997). The results of the direct numerical simulations could suggest that apparently chaotic trajectories are found experimentally because the dynamics in the transition range is very sensitive to experimental noise. However, it could also be that the transition between fluttering and tumbling in some cases, e.g. at higher values of the Reynolds number, takes place through a sequence of chaotic solutions.

3. Phenomenological model of a falling card

3.1. *Governing differential equations*

To gain further insight into the nature of the transition between fluttering and tumbling we consider a phenomenological model of the card aerodynamics based on ordinary differential equations (ODEs) introduced by Pesavento & Wang (2004). We

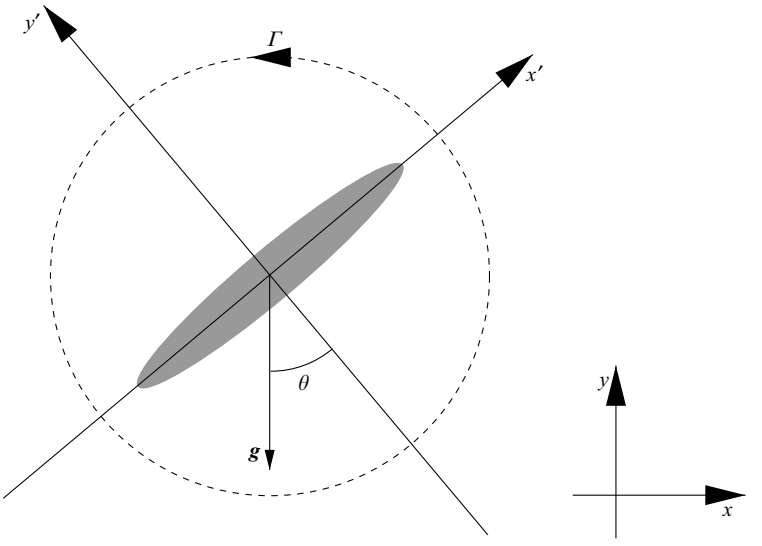

FIGURE 2. The velocity components $v_{x'}$ and $v_{y'}$ in the laboratory reference frame are defined with respect to the coordinate system following the rotation of the card, whereas v_x and v_y are defined with respect to the fixed coordinate system in the laboratory reference frame.

aim to identify the bifurcation between fluttering and tumbling in the ODE model and to quantify the divergence of the period of oscillation at the transition point.

We model the two-dimensional dynamics of a rigid card falling in a fluid by ordinary differential equations with fluid force contributions from added mass, lift, and drag. We apply a quasi-steady approximation in which the fluid forces are expressed in terms of the kinematic variables of the card alone. The Reynolds number based on the semi-major axis and the average descent velocity of a paper card falling in air is of the order of 10^3. The quadratic lift and drag terms in the model are designed to describe the aerodynamics at such intermediate Reynolds numbers between 10^2 and 10^3. We assume that the card has elliptical cross-section with half-major axis, a, and half-minor axis, b. We write the model in the coordinate system co-rotating with the card, and we define the angle θ and the components of the centre of mass velocity $v_{x'}$ and $v_{y'}$ as shown in figure 2. We have $v_x = v_{x'}\cos\theta - v_{y'}\sin\theta$ and $v_y = v_{x'}\sin\theta + v_{y'}\cos\theta$, where v_x is the horizontal velocity component and v_y is the vertical velocity component.

Our model consists of the following set of coupled ordinary differential equations:

$$(m + m_{11})\dot{v}_{x'} = (m + m_{22})\dot{\theta} v_{y'} - \rho_f \Gamma v_{y'} - \pi(\rho_s - \rho_f)abg\sin\theta - F^{\nu}_{x'}, \tag{3.1}$$

$$(m + m_{22})\dot{v}_{y'} = -(m + m_{11})\dot{\theta} v_{x'} + \rho_f \Gamma v_{x'} - \pi(\rho_s - \rho_f)abg\cos\theta - F^{\nu}_{y'}, \tag{3.2}$$

$$(I + I_a)\ddot{\theta} = (m_{11} - m_{22})v_{x'}v_{y'} - \tau^{\nu}. \tag{3.3}$$

The lift is orthogonal to the direction of motion and proportional to the circulation, $\Gamma = \Gamma(v_{x'}, v_{y'}, \dot{\theta})$, the drag, $\boldsymbol{F}^{\nu} = \boldsymbol{F}^{\nu}(v_{x'}, v_{y'}, \dot{\theta})$, is opposite to the direction of motion, and the dissipative torque, $\tau^{\nu} = \tau^{\nu}(v_{x'}, v_{y'}, \dot{\theta})$, is opposite to the direction of rotation.

We let m and I denote the mass and the moment of inertia per unit length:

$$m = \pi\rho_s ab, \qquad I = \tfrac{1}{4}\pi\rho_s ab(a^2 + b^2). \tag{3.4}$$

From inviscid theory (Sedov 1965) we have the added mass coefficients m_{11} and m_{22}, and the added moment of inertia, I_a, for the elliptical object:

$$m_{11} = \pi\rho_f b^2, \qquad m_{22} = \pi\rho_f a^2, \qquad I_a = \tfrac{1}{8}\pi\rho_f (a^2 - b^2)^2. \tag{3.5}$$

In the absence of viscous effects the model reduces to Kirchhoff's differential equations for a solid body in an inviscid and irrotational flow. In Kirchhoff's equations the fluid circulation has an arbitrary constant value. For discussion and analysis of Kirchhoff's equations see Lamb (1945), Kozlov (1989), and Aref & Jones (1993).

3.2. *Circulation and lift*

The current model of the fluid circulation was developed based on recent direct numerical simulations by Pesavento & Wang (2004) and experiments by Andersen *et al.* (2005). We found that the circulation for fluttering and tumbling cards in the Reynolds number range between 10^2 and 10^3 depends on both the translational speed and the angular velocity of the card:

$$\Gamma = \pm C_T a \sqrt{v_{x'}^2 + v_{y'}^2} \sin 2\alpha + 2C_R a^2 \dot{\theta}, \tag{3.6}$$

where α is the angle of attack and C_T and C_R are dimensionless coefficients. The sign of the translational term depends on the direction of motion and the orientation of the card. In terms of $v_{x'}$, $v_{y'}$, and $\dot{\theta}$ we have

$$\Gamma = -2C_T a \, \frac{v_{x'} v_{y'}}{\sqrt{v_{x'}^2 + v_{y'}^2}} + 2C_R a^2 \dot{\theta}. \tag{3.7}$$

The translational term reduces to the Kutta–Joukowski lift at low angles of attack and takes stall into account at high angles of attack. This model of the circulation is different from previous models, where either an arbitrary constant circulation was assumed (Mahadevan 1996) or the classical low angle of attack Kutta–Joukowski lift was applied (Tanabe & Kaneko 1994; Belmonte *et al.* 1998). The translational and the rotational contribution to the circulation both play important roles as discussed in Pesavento & Wang (2004) and Andersen *et al.* (2005). Translational lift provides an important contribution to the fluid forces during the gliding segments in fluttering as illustrated in figure 1(*a*), whereas rotational lift is the dominant lift mechanism in tumbling. The centre of mass of the plate would not elevate at the turning points as illustrated in figure 1(*d*) without the rotational lift term.

3.3. *Drag and dissipative torque*

The drag and the dissipative torque depend on the Reynolds number. We follow Wang, Birch & Dickinson (2004) and in the range of intermediate to high Reynolds number we apply a quadratic drag with the following dependence on the angle of attack:

$$\begin{aligned} \boldsymbol{F}^v &= \rho_f a (A - B\cos 2\alpha) \sqrt{v_{x'}^2 + v_{y'}^2} (v_{x'}, v_{y'}) \\ &= \rho_f a \left[A - B \frac{v_{x'}^2 - v_{y'}^2}{v_{x'}^2 + v_{y'}^2} \right] \sqrt{v_{x'}^2 + v_{y'}^2} (v_{x'}, v_{y'}), \end{aligned} \tag{3.8}$$

where A and B are dimensionless constants. For the dissipative torque we use an expansion to second order in the angular velocity:

$$\tau^{v} = \pi\rho_f a^4 \left[\frac{U}{L}\mu_1 + \mu_2|\dot{\theta}|\right]\dot{\theta}, \tag{3.9}$$

where L is the characteristic length scale, U is the characteristic velocity scale (see the discussion in § 4), and μ_1 and μ_2 are dimensionless constants. The fluid torque model is compared with the measured fluid torque and the modelling of the dissipative torque term is discussed in Andersen *et al.* (2005).

The Reynolds number enters the model implicitly through the values of the non-dimensional coefficients C_T, C_R, A, B, μ_1, and μ_2. In the following we shall use lift and drag coefficients from the literature (Wang *et al.* 2004), whereas we will fix the coefficients for the dissipative torque so that the time scale for the oscillatory motion is correct and leads to qualitatively correct solutions with periodic fluttering and periodic tumbling. We conjecture that out of the six non-dimensional coefficients the two dissipative torque coefficients depend most sensitively on the Reynolds number, and that μ_1 and μ_2 increase with decreasing Reynolds number corresponding to an increase in the damping of the oscillatory motion with decreasing Reynolds number.

3.4. *Validity of the quasi-steady approximation*

The quasi-steady force model was compared with measured fluid forces on freely falling plates in the quasi-two-dimensional experiment by Andersen *et al.* (2005). It was found that the model captures the main features of the measured fluid forces for both fluttering, tumbling, and trajectories in the transition region between fluttering and tumbling with Reynolds number between 10^2 and 10^3. There are two main types of effects which are not accounted for in the quasi-steady approximation, i.e. unsteady corrections due to acceleration and effects due to the interaction of the card with existing vortex structures. The first type of unsteady effect includes development of lift during translational acceleration from rest at low angle of attack (Wagner 1925) and unsteady forces due to vortex formation at both leading and trailing edges during translational accelerating at high angle of attack (Pullin & Wang 2004). The second type of unsteady effect can be significant when the quasi-steady approximation is applied to problems like flapping flight in which a wing is oscillated back and forth and moves into its own wake (Dickinson, Lehmann & Sane 1999). However, a freely falling card does not interact with its own wake and such effects are of little significance in the present study.

4. Non-dimensional equations

We write the governing equations (3.1)–(3.3) in dimensionless form using the length scale, L, and the velocity scale, U, which we define by the expressions

$$L = a, \qquad U = \sqrt{(\rho_s/\rho_f - 1)gb}. \tag{4.1}$$

The average terminal velocity, U, is estimated by balancing gravity with a quadratic drag. Three non-dimensional parameters can be constructed from the six dimensional quantities described in the introduction. We follow Willmarth *et al.* (1964) and apply the thickness-to-width ratio, $\beta = b/a$, the dimensionless moment of inertia

$$I^* = \frac{\rho_s b}{\rho_f a}, \tag{4.2}$$

and the Reynolds number based on the semi-major axis and the terminal velocity

$$Re = \frac{aU}{\nu}. \tag{4.3}$$

Using the characteristic scales and the three non-dimensional numbers we obtain the following non-dimensional governing equations:

$$(I^* + \beta^2)\dot{v}_{x'} = (I^* + 1)\dot{\theta} v_{y'} - \Gamma v_{y'} - \sin\theta - F^{\nu}_{x'}, \tag{4.4}$$

$$(I^* + 1)\dot{v}_{y'} = -(I^* + \beta^2)\dot{\theta} v_{x'} + \Gamma v_{x'} - \cos\theta - F^{\nu}_{y'}, \tag{4.5}$$

$$\tfrac{1}{4}\left[I^*(1+\beta^2) + \tfrac{1}{2}(1-\beta^2)^2\right]\ddot{\theta} = (\beta^2 - 1)v_{x'}v_{y'} - \tau^{\nu}, \tag{4.6}$$

where we differentiate with respect to the non-dimensional time and use $v_{x'}$, $v_{y'}$, Γ, $\boldsymbol{F}^{\nu}$, and τ^{ν} to denote the non-dimensional quantities. We apply the lift and the drag (3.7)–(3.9) which are valid in the intermediate to high Re range and for which the coefficients depend implicitly on Re. In non-dimensional form we have

$$\Gamma = \frac{2}{\pi}\left[-C_T \frac{v_{x'}v_{y'}}{\sqrt{v_{x'}^2 + v_{y'}^2}} + C_R\dot{\theta}\right], \tag{4.7}$$

$$\boldsymbol{F}^{\nu} = \frac{1}{\pi}\left[A - B\frac{v_{x'}^2 - v_{y'}^2}{v_{x'}^2 + v_{y'}^2}\right]\sqrt{v_{x'}^2 + v_{y'}^2}(v_{x'}, v_{y'}), \tag{4.8}$$

$$\tau^{\nu} = [\mu_1 + \mu_2|\dot{\theta}|]\dot{\theta}. \tag{4.9}$$

In the following we investigate the dependence on the non-dimensional parameters and solve the equations numerically in the range of small thickness-to-width ratio.

5. Numerical solutions with small thickness-to-width ratio

5.1. *Small thickness-to-width ratio*

In the limit of small thickness-to-width ratio, $\beta \ll 1$, equations (4.4)–(4.6) reduce to

$$I^*\dot{v}_{x'} = (I^* + 1)\dot{\theta} v_{y'} - \Gamma v_{y'} - \sin\theta - F^{\nu}_{x'}, \tag{5.1}$$

$$(I^* + 1)\dot{v}_{y'} = -I^*\dot{\theta} v_{x'} + \Gamma v_{x'} - \cos\theta - F^{\nu}_{y'}, \tag{5.2}$$

$$\tfrac{1}{4}\left(I^* + \tfrac{1}{2}\right)\ddot{\theta} = -v_{x'}v_{y'} - \tau^{\nu}. \tag{5.3}$$

In this limit the model depends on Re and I^* alone in agreement with the phase diagrams measured by Willmarth *et al.* (1964), Smith (1971), and Field *et al.* (1997). We emphasize that the equations do not depend on the density ratio, but explicitly on the non-dimensional moment of inertia defined in equation (4.2).

5.2. *Numerical solutions*

Figure 3 shows numerical solutions of equations (5.1)–(5.3) supplemented by the terms (4.7)–(4.9) with $C_T = 1.2$, $C_R = \pi$, $A = 1.4$, and $B = 1.0$, see Wang *et al.* (2004). For the dissipative torque we set $\mu_1 = \mu_2 = 0.2$, which determines the time scale for the oscillations relative to the time scale characterizing the vertical descent and leads to solutions with periodic fluttering and periodic tumbling in qualitative agreement with the direct numerical solutions shown in figure 1.

Figure 3 shows periodic fluttering for $I^* = 1.1$, period-one tumbling for $I^* = 1.4$, period-two tumbling for $I^* = 1.45$, periodic mixture of fluttering and tumbling for $I^* = 1.6$, chaotic dynamics for $I^* = 2.2$, and small-amplitude broadside-on fluttering

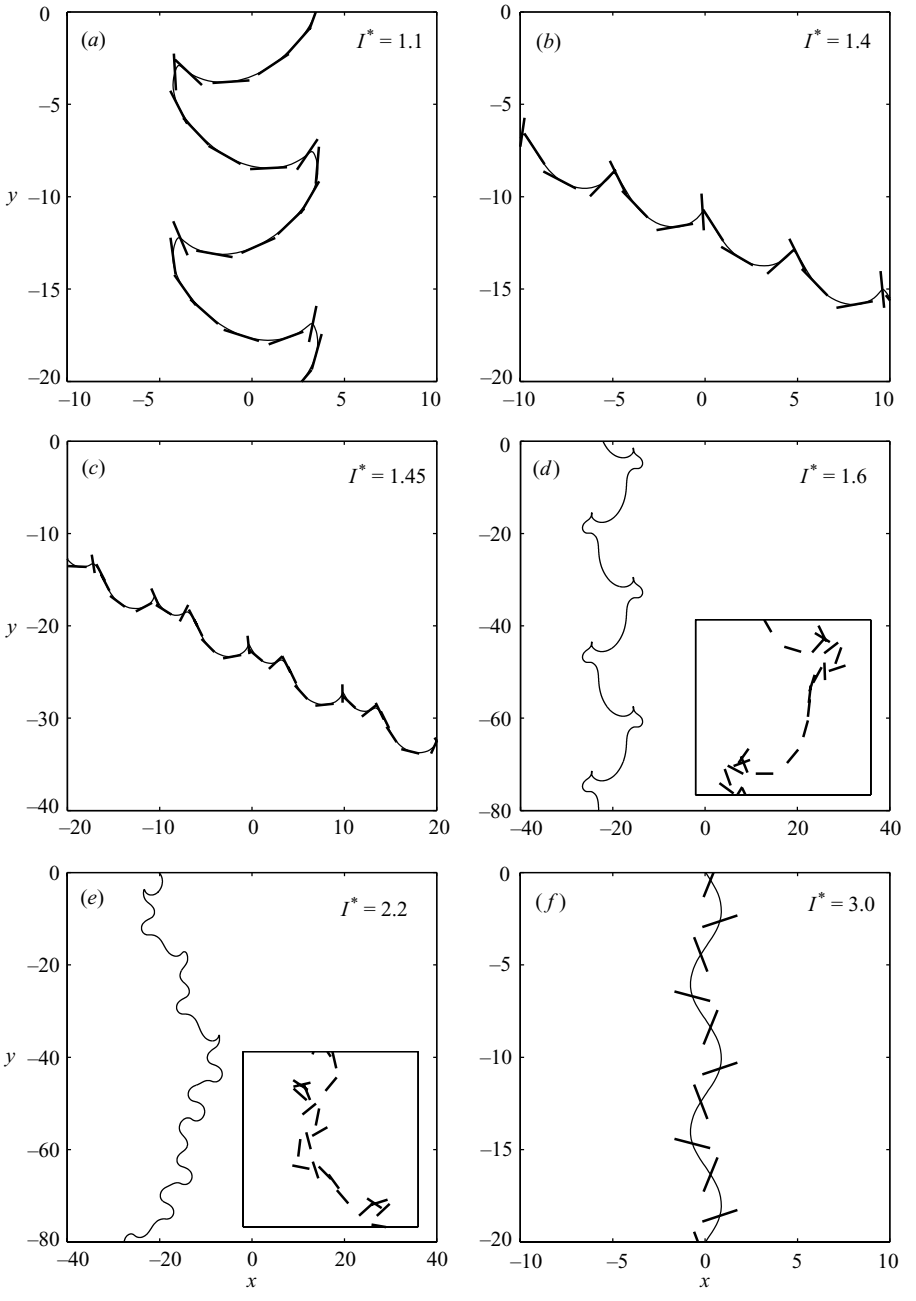

FIGURE 3. Numerical solutions of the non-dimensional equations (5.1)–(5.3) showing the card trajectories: (*a*) periodic fluttering for $I^* = 1.1$, (*b*) period-one tumbling for $I^* = 1.4$, (*c*) period-two tumbling for $I^* = 1.45$, (*d*) periodic mixture of fluttering and tumbling for $I^* = 1.6$, (*e*) chaotic dynamics for $I^* = 2.2$, and (*f*) small-amplitude broadside-on fluttering for $I^* = 3.0$.

for $I^* = 3.0$. As expected from the phase diagram measured by Willmarth *et al.* (1964) and the study by Belmonte *et al.* (1998) we observe a transition from fluttering to tumbling with increasing I^* as shown in figures 3(*a*) and 3(*b*). The periodic solutions are independent of the initial conditions and follow after short transients.

The fluttering with $I^* = 1.1$ and the tumbling with $I^* = 1.4$ alternate between gliding at low angle of attack and fast rotational motion and centre of mass elevation at the turning points in agreement with the direct numerical simulations by Pesavento & Wang (2004) and the experiment by Andersen *et al.* (2005). We find a period-doubling bifurcation between $I^* = 1.4$ and $I^* = 1.45$, and we note that the typical tumbling motion has a period-two structure as illustrated by the direct numerical solution shown in figure 1(*d*).

With $I^* = 1.6$ we find a periodic solution in which the card displays a mixture of fluttering and tumbling, and with $I^* = 2.2$ we find a chaotic solution with a maximum Lyapunov exponent of $\lambda_{max} = 0.13 \pm 0.01$. Chaotic solutions, for which the solution with $I^* = 2.2$ is a typical example, are found with $\mu_1 = \mu_2 = 0.2$ and I^* in the range between 1.8 and 2.8 as shown in figure 4(*b*) below. The card in figure 3(*f*) oscillates about the broadside-on fixed point. The broadside-on fixed point becomes stable and the oscillations are damped out if the dissipative torque is increased and the characteristic dissipative time scale for the decay of angular momentum is decreased. In the following we describe this bifurcation and the bifurcation between fluttering and tumbling.

6. Fixed points and bifurcations

6.1. *Transition between steady descent and oscillatory motion*

The differential equations have four steady solutions in which the card falls vertically and gravity is balanced by drag, i.e. two fixed points for which the card falls edge on:

$$\begin{bmatrix} v_{x'} \\ v_{y'} \\ \theta \\ \dot{\theta} \end{bmatrix} = \begin{bmatrix} \mp\sqrt{\dfrac{\pi}{A-B}} \\ 0 \\ \frac{1}{2}\pi,\ \frac{3}{2}\pi \\ 0 \end{bmatrix} = \begin{bmatrix} \mp V \\ 0 \\ \frac{1}{2}\pi,\ \frac{3}{2}\pi \\ 0 \end{bmatrix}, \tag{6.1}$$

and two fixed points for which the face of the card is normal to the direction of motion:

$$\begin{bmatrix} v_{x'} \\ v_{y'} \\ \theta \\ \dot{\theta} \end{bmatrix} = \begin{bmatrix} 0 \\ \mp\sqrt{\dfrac{\pi}{A+B}} \\ 0,\ \pi \\ 0 \end{bmatrix} = \begin{bmatrix} 0 \\ \mp W \\ 0,\ \pi \\ 0 \end{bmatrix} \tag{6.2}$$

Figure 4(*a*) illustrates the edge-on and the broadside-on steady solutions. We use V and W to denote the edge-on descent speed and the broadside-on descent speed, respectively. In the following we obtain the phase diagram for the system (5.1)–(5.3) in the I^* versus μ_1 plane and show that the transition between steady descent and oscillatory motion and the transition between fluttering and tumbling are related to the fixed points.

Figure 4(*b*) shows the phase diagram in the I^* versus μ_1 plane with fluttering, tumbling, and steady broadside-on descent as we vary I^*, μ_1, and μ_2 while keeping $\mu_1 = \mu_2$ and C_T, C_R, A, and B fixed. The transition between steady broadside-on descent and oscillatory motion takes place as the broadside-on fixed point goes from being stable to being unstable via a Hopf bifurcation at the bifurcation curve:

$$\mu_1 = \frac{1}{4}\sqrt{\frac{3}{5\pi}}\frac{2I^*+1}{I^*-1}. \tag{6.3}$$

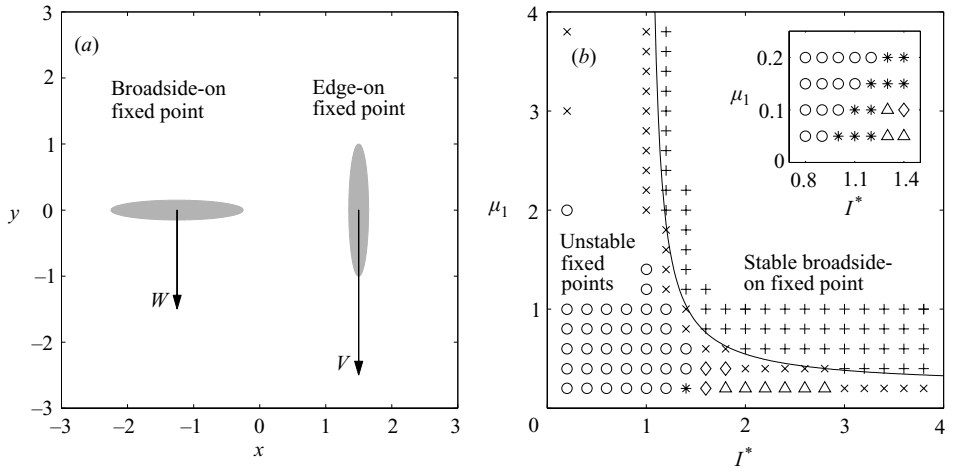

FIGURE 4. (*a*) Fixed points and descent velocities. (*b*) Phase diagram in the I^* versus μ_1 plane with the inset showing a magnification of the transition region between periodic fluttering and periodic tumbling. Numerical solutions of equations (5.1)–(5.3) and stability boundary for the broadside-on fixed point (solid curve). Periodic fluttering (circles), steady broadside-on descent (plus signs), periodic broadside-on fluttering (crosses), periodic tumbling (stars), periodic mixture of fluttering and tumbling (diamonds), and chaos (triangles).

The solid line in figure 4(*b*) shows the bifurcation curve which separates solutions with steady broadside-on descent and solutions with oscillatory motion. We find numerically that the size of the limit cycle grows continuously from zero and that the oscillation frequency in the neighbourhood of the bifurcation curve is equal to the absolute value of the imaginary parts of the complex-conjugate eigenvalues along the bifurcation curve. These numerical results indicate that the Hopf bifurcation is supercritical.

The edge-on fixed point is unstable for all values of I^* and μ_1 since the $v_{x'}v_{y'}$-term in equation (5.3) acts to rotate the card in the same direction as any small perturbation away from the edge-on orientation. For the broadside-on fixed point the $v_{x'}v_{y'}$-term instead acts in the opposite direction to any small perturbation away from the broadside-on orientation and the fixed point is stable if I^* and μ_1 are sufficiently large.

6.2. *Transition between fluttering and tumbling*

The transition from fluttering to tumbling with increasing I^* and constant μ_1 and μ_2 shown in figures 3(*a*) and 3(*b*) is a heteroclinic bifurcation. The critical value of I^* increases when the dissipative torque is increased as shown in the inset of figure 4(*b*). Figure 5(*a*) shows numerical solutions of equations (5.1)–(5.3) in the vicinity of the bifurcation point $I^*_C \approx 1.2191$. The cards fall edge on and accelerate downward for approximately 25 card widths, and when the cards reach the maximum descent speed they flutter for $I^* = 1.2190$ and tumble for $I^* = 1.2192$. Figure 5(*b*) shows the phase-space trajectory for fluttering projected onto the three-dimensional space spanned by $v_{y'}$, θ, and ω, where we use the definition $\omega \equiv \dot{\theta}$. The trajectory spirals in toward one of the edge-on fixed points, moves away on the unstable manifold, and follows the heteroclinic orbit to the other edge-on fixed point. Figure 5(*c*) shows the phase-space trajectory in the neighbourhood of the edge-on fixed point. The linearized equation for $v_{x'}$ in the neighbourhood of the edge-on fixed point is decoupled from the three

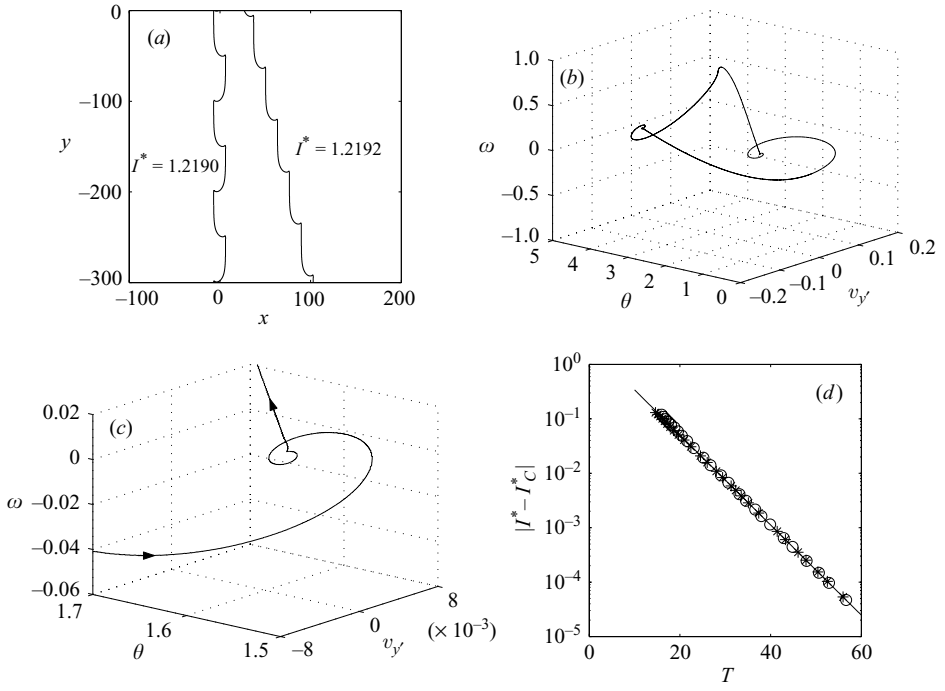

FIGURE 5. The transition between fluttering and tumbling. (*a*) Numerical solutions of equations (5.1)–(5.3) below and above the bifurcation point $I_C^* \approx 1.2191$; (*b*) and (*c*) the phase-space trajectory for $I^* = 1.2190$ projected onto the space spanned by $v_{y'}$, θ, and ω (with $\omega \equiv \dot{\theta}$); and (*d*) the logarithmic divergence of the period of oscillation, T, in the neighbourhood of I_C^*: theoretical prediction (solid line) and numerical results with $I^* < I_C^*$ (circles) and $I^* > I_C^*$ (stars).

other linearized equations and the direction is stable, $\lambda_s = -0.5854$. The three other linearized equations are coupled and the eigenvalue equation has one positive real root, $\lambda_u = 0.3813$, and a pair of complex-conjugate roots with negative real part, $\lambda_\pm = -0.9861 \pm \mathrm{i}2.5949$. The dynamics in the three-dimensional space spanned by $v_{y'}$, θ, and ω therefore resembles Silnikov's phenomenon (Guckenheimer & Holmes 1983). In general the existence of a Silnikov bifurcation opens the possibility for chaos, but in the present case the solutions in the vicinity of the bifurcation point are not chaotic. However, the solutions close to the bifurcation are sensitive to noise, and the numerical integration must be carried out with high accuracy in the transition region.

The period of oscillation, T, diverges logarithmically at the bifurcation point:

$$T = T_0 + \frac{2}{\lambda_u} \log \frac{1}{|I^* - I_C^*|}. \tag{6.4}$$

The logarithmic prefactor is inversely proportional to λ_u evaluated at the bifurcation point, and the logarithmic divergence of T is a characteristic signature of homoclinic and heteroclinic bifurcations (Gaspard 1990). The factor of 2 in equation (6.4) appears because the saddle fixed point is encountered twice during each full period of oscillation as shown in figure 5(*b*). Figure 5(*d*) shows a semi-logarithmic plot of $|I^* - I_C^*|$ versus T obtained numerically with $I^* < I_C^*$ (circles) and $I^* > I_C^*$ (stars). The numerical results are in perfect agreement with the theoretical prediction (solid line) with the eigenvalue $\lambda_u = 0.3813$ and the fit parameter $T_0 = 4.3629$.

7. Summary and discussion

We have presented direct numerical simulations of the two-dimensional Navier–Stokes equation for the flow around a card falling freely in a fluid. We have found a transition between fluttering and tumbling by changing the thickness-to-width ratio and thereby the non-dimensional moment of inertia. In the wide transition region we have observed periodic solutions in which the cards flutter periodically but tumble once between consecutive turning points, and we have found that the period of oscillation diverges.

To further investigate the transition between fluttering and tumbling we have analysed a phenomenological model with both translational and rotational lift for a rigid card falling in air, and we have shown that the model depends on the thickness-to-width ratio, the dimensionless moment of inertia, and the Reynolds number. We have shown that the transition between stable broadside-on descent and oscillatory motion is a supercritical Hopf bifurcation. By investigating the numerical solutions of the phenomenological model we have shown that the transition between fluttering and tumbling in the model is a heteroclinic bifurcation which leads to a logarithmic divergence of the period of oscillation with a prefactor that is inversely proportional to the eigenvalue of the unstable mode at the edge-on saddle fixed points.

The bifurcation scenario of the phenomenological model agrees with important features of the transition between fluttering and tumbling observed in the direct numerical simulations, including the long vertical gliding segments and the divergence of the period of oscillation. However, the phenomenological model predicts a sharp transition between fluttering and tumbling, whereas the direct numerical simulations show a wide transition region with solutions that are mixtures of fluttering and tumbling. Such solutions are also found in the phenomenological model, but at larger values of the dimensionless moment of inertia, and they are apparently not related to the transition between fluttering and tumbling. The direct numerical simulations show that the transition between fluttering and tumbling does not have to take place through a sequence of chaotic solutions, but they do not exclude the possibility of chaos at the transition, e.g. at higher Reynolds numbers. We hope that the present work will encourage further studies to elucidate the bifurcation structure of the Navier–Stokes equation for the flow around a falling card.

We thank John Guckenheimer, Sovan Lal Das, Lakshminarayanan Mahadevan, and Richard Rand for many valuable comments and suggestions. This work was supported by NSF, ONR, AFOSR, and the Packard Foundation.

REFERENCES

Andersen, A., Pesavento, U. & Wang, Z. J. 2005 Unsteady aerodynamics of fluttering and tumbling plates. *J. Fluid Mech.* **541**, 65–90.

Aref, H. & Jones, S. W. 1993 Chaotic motion of a solid through ideal fluid. *Phys. Fluids* A **5**, 3026–3028.

Belmonte, A., Eisenberg, H. & Moses, E. 1998 From flutter to tumble: inertial drag and Froude similarity in falling paper. *Phys. Rev. Lett.* **81**, 345–348.

Dickinson, M. H., Lehmann, F.-O. & Sane, S. P. 1999 Wing rotation and the aerodynamic basis of insect flight. *Science* **284**, 1954–1960.

Field, S. B., Klaus, M., Moore, M. G. & Nori, F. 1997 Chaotic dynamics of falling disks. *Nature* **388**, 252–254.

Gaspard, P. 1990 Measurement of the instability rate of a far-from-equilibrium steady state at an infinite period bifurcation. *J. Phys. Chem.* **94**, 1–3.

Guckenheimer, J. & Holmes, P. 1983 *Nonlinear Oscillations, Dynamical Systems, and Bifurcations of Vector Fields*. Springer.

Kozlov, V. V. 1989 Heavy rigid body falling in an ideal fluid. *Mech. Solids* **24**, 9–17.

Lamb, H. 1945 *Hydrodynamics*. Dover.

Mahadevan, L. 1996 Tumbling of a falling card. *C. R. Acad. Sci. Paris* **323**, 729–736.

Mahadevan, L., Ryu, W. S. & Samuel, A. D. T. 1999 Tumbling cards. *Phys. Fluids* **11**, 1–3.

Maxwell, J. C. 1854 On a particular case of the descent of a heavy body in a resisting medium. *Camb. Dublin Math. J.* **9**, 145–148.

Pesavento, U. & Wang, Z. J. 2004 Falling paper: Navier-Stokes solutions, model of fluid forces, and center of mass elevation. *Phys. Rev. Lett.* **93**, 144501.

Pullin, D. I. & Wang, Z. J. 2004 Unsteady forces on an accelerating plate and application to hovering insect flight. *J. Fluid Mech.* **509**, 1–21.

Sedov, L. I. 1965 *Two-Dimensional Problems in Hydrodynamics and Aerodynamics*. Interscience.

Smith, E. H. 1971 Autorotating wings: an experimental investigation. *J. Fluid Mech.* **50**, 513–534.

Tanabe, Y. & Kaneko, K. 1994 Behavior of a falling paper. *Phys. Rev. Lett.* **73**, 1372–1375.

Wagner, H. 1925 Über die Entstehung des dynamischen Auftriebes von Tragflügeln. *Z. Angew. Math. Mech.* **5**, 17–35.

Wang, Z. J. 2000 Vortex shedding and frequency selection in flapping flight. *J. Fluid Mech.* **410**, 323–341.

Wang, Z. J., Birch, J. M. & Dickinson, M. H. 2004 Unsteady forces and flows in low Reynolds number hovering flight: two-dimensional computations *vs* robotic wing experiments. *J. Expl Biol.* **207**, 449–460.

Willmarth, W. W., Hawk, N. E. & Harvey, R. L. 1964 Steady and unsteady motions and wakes of freely falling disks. *Phys. Fluids* **7**, 197–208.